



This is a repository copy of *Low-temperature, scalable, reactive deposition of tin oxide for perovskite solar cells*.

White Rose Research Online URL for this paper:

<https://eprints.whiterose.ac.uk/188682/>

Version: Published Version

Article:

Blackburn, D., Routledge, T.J., O’Kane, M. et al. (6 more authors) (2022) Low-temperature, scalable, reactive deposition of tin oxide for perovskite solar cells. *Solar RRL*, 6 (8). 2200263.

<https://doi.org/10.1002/solr.202200263>

Reuse

This article is distributed under the terms of the Creative Commons Attribution (CC BY) licence. This licence allows you to distribute, remix, tweak, and build upon the work, even commercially, as long as you credit the authors for the original work. More information and the full terms of the licence here:

<https://creativecommons.org/licenses/>

Takedown

If you consider content in White Rose Research Online to be in breach of UK law, please notify us by emailing eprints@whiterose.ac.uk including the URL of the record and the reason for the withdrawal request.



eprints@whiterose.ac.uk
<https://eprints.whiterose.ac.uk/>

Low-Temperature, Scalable, Reactive Deposition of Tin Oxide for Perovskite Solar Cells

Dominic Blackburn, Thomas J. Routledge, Mary O’Kane, Elena J. Cassella, Onkar S. Game, Thomas E. Catley, Christopher J. Wood, Trevor McArdle, and David George Lidzey*

Tin oxide (SnO_x) electron-extraction layers are fabricated via a reactive electron-beam evaporation process from a metal source under a partial pressure of oxygen. These are then used in standard (n-i-p) architecture perovskite solar cells and achieve power conversion efficiencies up to 19.3%. The SnO_x deposition process is performed onto substrates maintained at low temperature compared to similar techniques, with films not requiring any subsequent high-temperature post-deposition annealing. This demonstrates the potential compatibility of reactive electron-beam evaporation with roll-to-roll processing onto flexible polymeric substrates.


1. Introduction

Interest in perovskite solar cells (PSCs) has increased greatly over the recent years due to the rapid improvement in photovoltaic performance. The first reported perovskite photovoltaic devices had a power conversion efficiency (PCE) of 3.8%, which then increased as a result of intensive research and development to now exceed 25%.^[1–4] This increase in device performance has been driven by the high absorption coefficient, long charge-carrier diffusion length, tunable optical bandgap, and low defect density of metal-halide perovskites.^[5–16] Indeed, the photovoltaic performance of lab-scale PSCs is now comparable to crystalline silicon cells. However, much development is still required to develop perovskite manufacturing processes to compete commercially with silicon.

The first reports of PSCs were based on structures developed from dye-sensitized solar cells and used an n-i-p architecture.

D. Blackburn, T. J. Routledge, M. O’Kane, E. J. Cassella, O. S. Game, T. E. Catley, D. G. Lidzey
Department of Physics & Astronomy
University of Sheffield
Sheffield S3 7RH, UK
E-mail: d.g.lidzey@sheffield.ac.uk

C. J. Wood, T. McArdle
Power Roll Limited
PV Development
Seaham SR7 9DR, UK

 The ORCID identification number(s) for the author(s) of this article can be found under <https://doi.org/10.1002/solr.202200263>.

© 2022 The Authors. Solar RRL published by Wiley-VCH GmbH. This is an open access article under the terms of the Creative Commons Attribution License, which permits use, distribution and reproduction in any medium, provided the original work is properly cited.

DOI: 10.1002/solr.202200263

Initially, devices used an electron transport layer (ETL) based on mesoporous titanium dioxide (m-TiO₂), which is enhanced by the addition of a compact TiO₂ layer incorporated beneath the m-TiO₂ layer.^[17–21] However, it has been shown that TiO₂-based PSCs undergo degradation when exposed to UV light.^[22] The push for higher efficiencies and more stable devices has seen the exploration of numerous alternative metal oxides and organic thin films.^[23–27] In recent years, SnO₂ has been shown to be a particularly promising ETL due to its wide bandgap, high

optical transmission, high electron mobility, and a conduction band that is well aligned with common perovskite compositions.^[28–34]

A number of techniques have been explored to deposit SnO₂ ETLs, including chemical bath deposition (CBD), sol–gel conversion, atomic layer deposition (ALD), chemical vapor deposition (CVD), thermal evaporation, magnetron sputtering, pulsed laser deposition, colloidal nanoparticle routes, and electron-beam evaporation.^[35–38] However, many of these fabrication routes have potential manufacture scaling issues. For example, CBD requires an elevated temperature during the deposition or the application of a post-deposition sintering step making it incompatible with the sensitive polymeric substrates that are increasingly used in flexible photovoltaic applications.^[39] Recently, process temperatures below 100 °C have been demonstrated, however, these often require extended reaction times making them less suitable for mass production. They also require the use of highly acidic solutions, again making them unsuitable for combination with sensitive polymeric substrates.^[3,40]

Although high-quality layers can be deposited via ALD, the slow deposition rates and multiple cycles required to build up layers of the thickness required for high-performing devices are also barriers to rapid production.^[41–43] Furthermore, ALD processes can result in the generation of gaseous and corrosive by-products which can contaminate the substrate.

Colloidal SnO₂ nanoparticles have been successfully spin-cast on small area devices to produce high-performing PSCs and these have been deposited via slot-die, blade, and spray coating, demonstrating their potential scalability.^[33,44–51] However, such nanoparticle solutions usually contain residual organic ligands or stabilizers that cannot be removed by low-temperature annealing. As such their compatibility with polymeric substrates for roll-to-roll processing is questionable. In fact, some of the added stabilizers are known to reduce the stability of triple cation-based perovskites through the generation of undesirable metal halide salts.^[52]

Thermal evaporation, magnetron sputtering, pulsed laser deposition (PLD), and electron-beam evaporation have all been previously used to deposit SnO₂ for PSCs.^[53–57] These deposition techniques share broad similarities, with each having their own benefits and drawbacks, however, in each case, the source material for deposition has been stoichiometric SnO₂. This requirement can also result in production issues as the exposure of a stoichiometric source material to a laser, ion, or electron-beam quickly changes initial stoichiometry, even under oxygen partial pressures. This in turn can lead to a variation in the optoelectronic properties of the layer deposited during the deposition, leading to poor control over device properties.

In this article, we deposit SnO_x films using a process that utilizes metallic tin pellets as a source material which are evaporated using an electron-beam (Figure 1a). During the process, oxygen is fed into the chamber to maintain a constant partial pressure, oxidizing the vaporized metal as it is deposited. After deposition, the films are exposed to a UV–ozone treatment, which further increases the ratio of oxygen-to-tin in the film, improving the optical transmission and the functionality of the layer. The reactive electron-beam technique used here has been previously used to fabricate hole-selective nickel oxide and electron-selective titanium dioxide from metal sources, demonstrating its broad applicability to deposit a range of metal oxide thin films for optoelectronics.^[58] Reactive electron-beam deposition of metal oxides is inherently low-cost in nature and combines both reduced substrate temperature and high-speed deposition.^[59–61] It is, therefore, well suited for use on polymeric substrates as part of a roll-to-roll process. Using this technique, we fabricate standard architecture (n-i-p) PSCs with a SnO_x electron-transporting layer and report a champion PCE of 19.3%. This is benchmarked against devices that incorporate a SnO₂ ETL prepared from colloidal SnO₂ nanoparticles, with similar performance metrics demonstrated.

2. Results

SnO_x films were deposited using a low-temperature reactive electron-beam process incorporating a post-deposition UV–ozone treatment. The composition, transmission, surface topography, and crystal morphology of representative thin films were

characterized, with properties compared both with and without the post-deposition UV–ozone treatment. Films were then utilized as the ETL in standard architecture (n-i-p) devices to extract performance metrics and external quantum efficiency (EQE) and compared with the equivalent devices prepared using nanoparticle SnO₂ ETL (np-SnO₂).

We first discuss the optical characterization of the reactive SnO_x (r-SnO_x) thin films. Here, films of 25 nm thickness were deposited on either quartz-coated glass (Figure 2a) or indium tin oxide (ITO) coated glass substrates (Figure S3, Supporting Information) at a partial pressure of 9×10^{-4} mbar oxygen and at a rate of 1.75 \AA s^{-1} (further details in supplemental). The thickness of this layer was chosen to closely replicate the thickness of films used as ETLs in optimized PSC devices. It was found that freshly deposited r-SnO_x films (without any post-deposition treatments) had good optical transparency but were slightly “gray” when inspected by the eye. Figure 2a shows the optical transmission of such films on quartz-coated glass. Here it can be seen that films have 75% transmission at 380 nm which increases to 90% at 498 nm and 95% at wavelengths beyond 605 nm. We have found that when these films are treated with UV–ozone for 20 min, they have enhanced levels of transparency with a transmission of 80% at 380 nm, 90% at 444 nm, and >95% at wavelengths longer than 519 nm. However, this is less than the transparency of films deposited from colloidal nanoparticle tin oxide solutions which have a transmission of >95% across the entire visible region.

It is apparent that the UV–ozone-treated r-SnO_x films have good optical transmissivity, however, the observed reduction in transmission (compared to films prepared from np-SnO₂) might lead to a relative reduction in photocurrent when they are used as an ETL in photovoltaic devices owing to parasitic optical absorption. To investigate this issue, measurements were repeated on ITO substrates (Figure S3, Supporting Information). Here we find that differences in transmission between np-SnO₂ and UVO-treated r-SnO_x films were significantly reduced at wavelengths <500 nm, with the transmission of the films being nearly identical at wavelengths >500 nm. This suggests that the use of r-SnO_x ETLs will have a relatively insignificant effect on photocurrent when they are incorporated as an ETL in PSC devices. We note that the transmission of np-SnO₂ films deposited on an ITO-coated substrate is higher than the transmission of

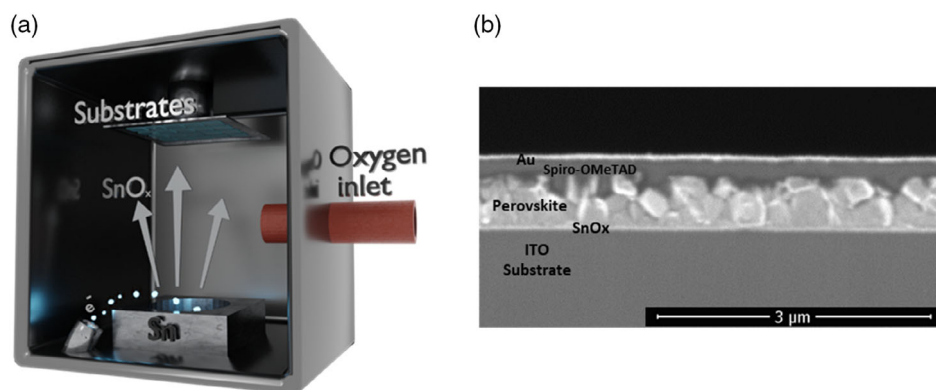


Figure 1. a) Schematic diagram of a reactive electron-beam deposition process. b) Cross-sectional scanning electron microscope (SEM) image of device featuring reactive SnO_x as the electron transport layer (ETL).

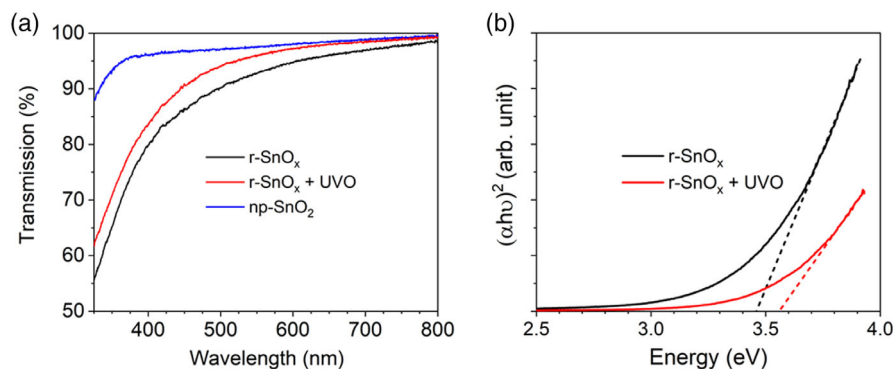


Figure 2. a) Transmission spectra of 25 nm r-SnO_x films on quartz with and without UV–ozone treatment compared with that of np-SnO₂. b) Tauc plot of r-SnO_x (85 nm thick film) with and without UV–ozone treatment.

uncoated ITO at certain wavelengths as ITO itself can act as an antireflective layer.

To further explore the effect of the UV–ozone treatment on r-SnO_x, we have deposited films having enhanced thickness (85 nm) on quartz substrates with transmission measurements then recorded. Here, it was found that such thicker films allowed the absorption edge to be more clearly identified than comparable transmission measurements made on device-appropriate (thinner) films (Figure S1, Supporting Information). Figure 2b shows a Tauc plot constructed from the transmission data, with data presented for an r-SnO_x film both with and without UV–ozone treatment. From this, we determine a bandgap for the untreated r-SnO_x film of 3.46 eV; a value that increased to 3.56 eV after the 20 min UV–ozone treatment. This increase in bandgap is consistent with the increase in optical transmission observed across the visible spectrum following UV–ozone treatment. We note that the bandgap of colloidal nanoparticle SnO₂ films has been determined to be 3.79 eV; a result that suggests the UV–ozone-treated r-SnO_x films explored here are likely to be sub-stoichiometric.

Figure 3a shows atomic force microscopy (AFM) topographs recorded from a bare ITO substrate and a 25 nm thick, UV–ozone-treated r-SnO_x film deposited on an ITO substrate. From these, we determine root mean squared (RMS) roughness values of (1.9 ± 0.10) nm and (2.6 ± 0.04) nm, respectively. Given the uncertainty in such measurements, and that we did not observe significant short-circuiting in our devices, we conclude

that the roughness of the ITO surface is not substantially modified by the deposition of the r-SnO_x.

To further characterize the structure of the films, X-Ray diffraction (XRD) measurements were recorded from the UV–ozone-treated r-SnO_x on quartz-coated glass substrates. A typical scattering spectrum is shown in Figure 3b. Here it is apparent that no sharp (crystalline) diffraction features are observed, rather the films appear largely amorphous. We note previous measurements have reported that the colloidal nanoparticle films are crystalline, with (110), (101), (200), (211), (310), and (301) scattering planes observed, indicating a tetragonal crystalline structure.^[33]

We have characterized the elemental composition and stoichiometry of our films using X-Ray photoelectron spectroscopy (XPS). Figure 4a shows the Sn 3d_{5/2} core lines recorded from a thin r-SnO_x film with 4b showing the equivalent spectra recorded from a similar film after UV–ozone treatment. It can be seen that the peak energy and linewidth of r-SnO_x films both before and after UV–ozone treatment are very similar, with peaks observed at 486.9 and 487.0 eV respectively. Such values closely match literature values for SnO₂ (486.7–487.0 eV) and np-SnO₂ (486.9 eV).^[62] We note, however, that the UV–ozone treatment affected the O1s signal which increased in relative intensity compared to the 3d_{5/2} peak and underwent some broadening (see Figure S2, Supporting Information) suggesting increased incorporation of oxygen into the film. We can estimate film stoichiometry by comparing the area of the O1s and Sn 3d_{5/2}

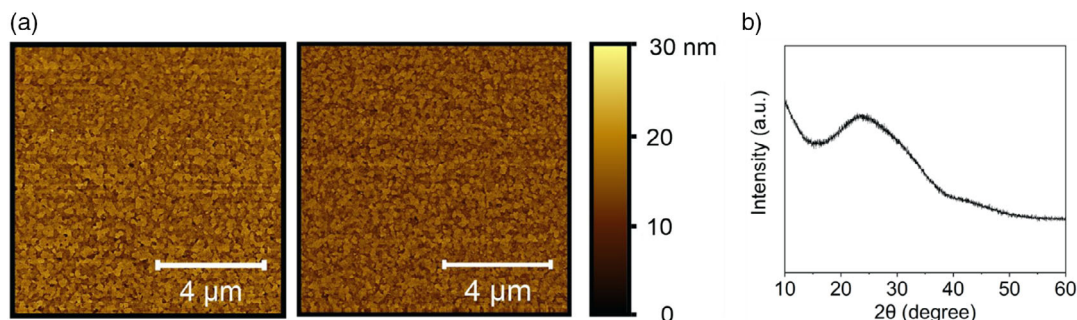


Figure 3. a) Atomic force microscopy (AFM) images of bare ITO substrate (left) and a 25 nm thick film of r-SnO_x on ITO (right). b) X-Ray diffraction (XRD) of r-SnO_x film after UV–ozone treatment.

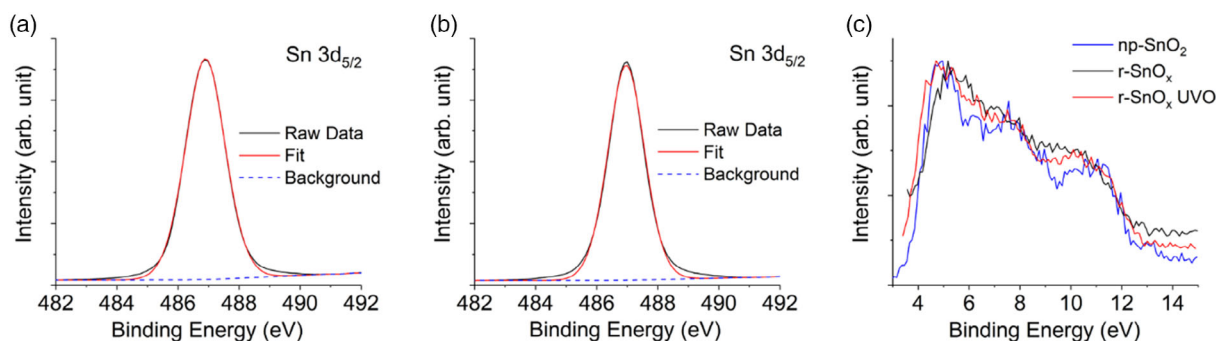


Figure 4. a) X-Ray photoelectron spectroscopy (XPS) of r-SnO_x. b) XPS of r-SnO_x with UV–ozone treatment. c) XPS valence spectra of r-SnO_x (with and without UV–ozone treatment) and np-SnO₂. Full spectra in Supporting Information.

peaks. This suggests an oxygen to tin ratio of 1.26 (SnO_{1.26}) in the untreated r-SnO_x film and 1.74 (SnO_{1.74}) in the UV–ozone-treated film. For completeness, if we apply the same technique to an np-SnO₂ film (Figure S2c, Supporting Information) we determine an oxygen to tin ratio of 2.03.

Figure 4c plots the tin valence spectra of the untreated r-SnO_x, UV–ozone-treated r-SnO_x, and colloidal np-SnO₂ films. Although the spectra are relatively noisy, it is apparent that there are three peaks in the UV–ozone-treated r-SnO_x and np-SnO₂ films whose intensity decreases with increasing binding energy; a result consistent with previous reports.^[63] Notably, however a peak around 8 eV is largely absent in the r-SnO_x film, with the valence spectra

being more similar to that of SnO.^[63] This further suggests that the untreated r-SnO_x film is sub-stoichiometric.

We now explore the application of the different SnO_x thin films as the ETL in a PSC. All devices were fabricated on ITO-coated glass substrates and utilized a spin-coated triple-cation perovskite annealed at 100 °C for 30 min under nitrogen. Hole extraction was achieved using a doped spiro-OMeTAD hole transport layer (HTL) and a top gold anode that was deposited by thermal evaporation (full details in supplemental). These devices had an active area defined by the anode and cathode-contact overlap of approximately 5 mm². An SEM cross-section through a typical device is shown in Figure 1b.

Table 1. Performance metrics from champion-device reverse sweeps. Mean and standard deviation shown in brackets. Further statistics on device performance metrics can be found in S5 and S6.

	PCE [%]	J_{sc} [mA cm ⁻²]	V_{oc} [V]	FF [%]
UVO treated r-SnO _x	19.3 (17.8 ± 1.4)	23.5 (22.6 ± 0.5)	1.14 (1.12 ± 0.02)	74.8 (71 ± 5)
np-SnO ₂	19.5 (18.4 ± 0.8)	23.1 (22.7 ± 0.2)	1.15 (1.13 ± 0.01)	75.0 (72 ± 3)

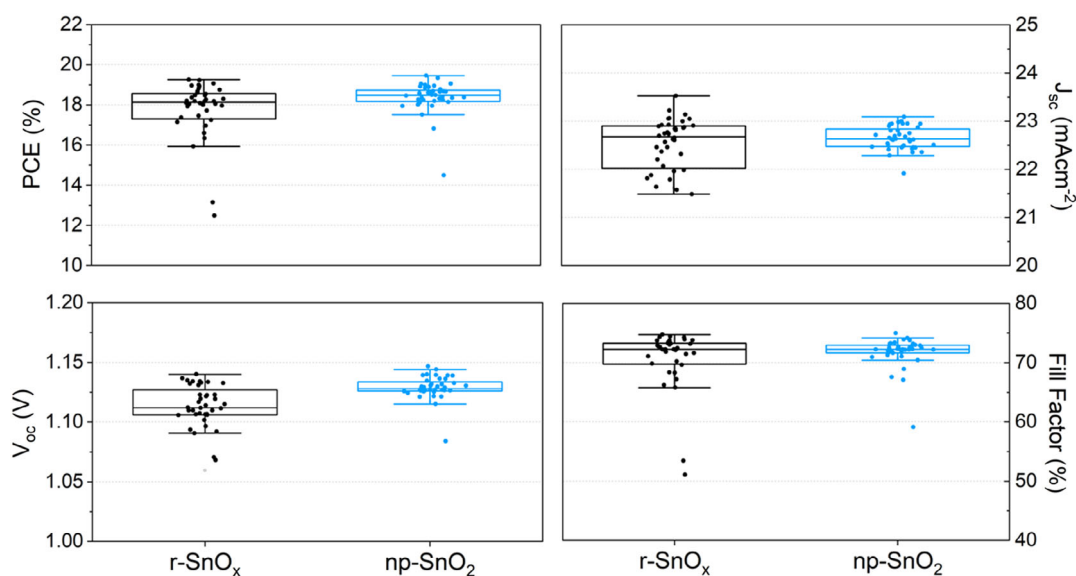


Figure 5. Boxplots showing distribution of performance metrics from equivalent devices made using np-SnO₂ and r-SnO_x.

Significantly, we find that devices made using untreated r-SnO_x films are largely nonfunctional, with negligible photocurrent recorded (see Figure S7, Supporting Information). However, when such films were exposed to a UV–ozone treatment for 20 min prior to perovskite deposition, device performance improved significantly. This can be seen in Figure 5 (Table 1) where we compare the reverse sweep metrics of devices incorporating the UV–ozone-treated r-SnO_x ETLs with those incorporating colloidal np-SnO₂. Here, we find the mean short circuit current density (J_{sc}) of both types of device to be near identical (22.6 ± 0.5 and 22.7 ± 0.2 mA cm⁻² respectively) despite the slightly lower transmission of the UV–ozone-treated r-SnO_x ETL film. We note however that the spread in J_{sc} is slightly narrower in devices incorporating the np-SnO₂ ETL. We also find that the mean open-circuit voltage (V_{oc}) and fill factor (FF) of the np-SnO₂ devices are slightly higher than those of the UV–ozone-treated r-SnO_x devices, being (1.11 ± 0.02 , 1.13 ± 0.01 V and 71 ± 5 , $72 \pm 3\%$ respectively). This results in a comparable but higher average PCE of $18.4 \pm 0.8\%$ for np-SnO₂ compared to $17.8 \pm 1.4\%$ for r-SnO_x.

We have also explored the fabrication of devices having a slightly larger active area (25 mm², but measured through an aperture mask of approximately 16 mm²). Here, Figure S9, Supporting Information, shows J – V sweeps of such larger area np-SnO₂ and r-SnO_x based devices, with PCEs determined of 16.8% and 15.2%, respectively. We expect that this reduction in PCE largely results from enhanced sheet resistance of the ITO contact which mainly reduces the fill factor.^[64]

Figure 6a plots the champion stabilized output of a UV–ozone-treated r-SnO_x ETL device, with Figure 6b plotting the forward and reverse J – V sweep from the champion stabilized pixel. Here it can be seen that, unlike np-SnO₂ devices which demonstrate negligible hysteresis (Figure S8, Supporting Information), the treated r-SnO_x device shows significant hysteresis. Specifically, we determine a V_{oc} (FF) value of 1.109 V (67%) for the forward sweep and 1.123 V (74%) for the reverse sweep, resulting in recorded PCE of 16.9% and 19.1%, respectively. However, when the same pixel was measured at the maximum power point, it stabilized to a PCE of 18.7%; a value only fractionally less than the reverse sweep performance. For completeness, Figure 6c shows the EQE of the same pixel together with the integrated J_{sc} obtained from the EQE. Here the integrated J_{sc} value of 21.5 mA cm⁻² is slightly lower than that taken from the reverse sweep value (22.9 mA cm⁻²). We note, however, that the difference of 1.4 mA cm⁻² observed here has been determined to be an acceptable level of mismatch, with multiple discrepancies between the measurement techniques speculated to explain this phenomenon.^[65]

Finally, we have explored the relative stability of devices based on utilizing np-SnO₂ and r-SnO_x ETLs. Here, devices were made as described earlier and exposed to 160 h of illumination in air using a light source approximating AM1.5, with periodic current–voltage sweeps made *in situ*. All devices were also characterized using a calibrated solar simulator before and after their respective light exposure. This was necessary, as the solar simulator and light source used in aging measurements had slightly different spectral characteristics. To accelerate the degradation processes, all devices remained unencapsulated during light exposure.

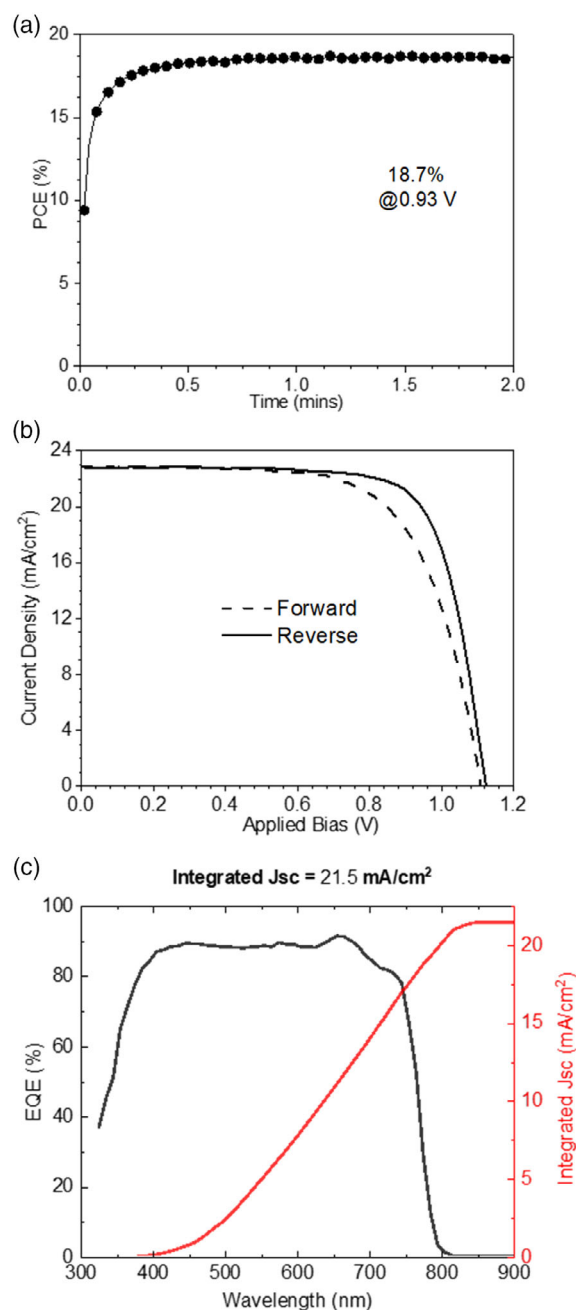


Figure 6. a) Champion stabilized power conversion efficiency (PCE) of UV–ozone-treated r-SnO_x device. b) J – V sweep of champion stabilized pixel. c) External quantum efficiency (EQE) measurement of the same pixel and integrated J_{sc} obtained from EQE.

Figure S11, Supporting Information, shows *in situ* PCE measurements recorded from both the np-SnO₂ and r-SnO_x devices made during light exposure. Figure S12, Supporting Information, shows the relative change in all device metrics recorded before and after the 160 h light exposure treatment. It can be seen that there are drops in all performance metrics for both types of the device after 160 h of light exposure, with these most notably occurring in J_{sc} . This suggests that the main

degradation process involved the perovskite light-harvesting layer. Indeed, a visual inspection following light exposure revealed that devices appeared “gray” on their light-exposed side, suggesting decomposition to lead iodide. Nevertheless, we find the r-SnO_x and np-SnO₂ devices to have a very similar level of stability, suggesting that the process used to deposit the SnO₂ film has little impact on device lifetime.

For completeness, unencapsulated devices were also stored under nitrogen in the dark (Figure S10, Supporting Information). Here, the r-SnO_x devices underwent very little reduction in their performance metrics after 12 days of storage. Interestingly, the np-SnO₂ devices had a larger spread in all performance metrics after storage, with some devices undergoing large losses in PCE. The reduced stability observed in some of the np-SnO₂ devices may occur as a result of excess potassium iodide, which is used as an additive to enhance the stability of the colloidal solution. This additive has previously been found to reduce the stability of mixed-halide perovskites through the formation of non-perovskite phases.^[52] This result suggests that the use of r-SnO_x deposited ETLs may well improve the long-term stability of PSC devices, however further measurements on fully encapsulated devices are needed to confirm this.

3. Discussion

We have analyzed the stoichiometry of tin oxide films prepared by reactive electron-beam deposition and by a conventional colloidal nanoparticle route via XPS and optical transmission measurements. XPS spectroscopy indicates an increase in the oxygen content of r-SnO_x films after a UV–ozone treatment, as has been previously demonstrated, with optical transmission measurements confirming the resulting changes in the electronic bandgap.^[66,67] We note, however, that XPS is a surface-sensitive technique that is only able to probe the composition of the top 10 nm of a film.^[68] As the tin oxide films used in devices were around 25 nm thick, XPS estimations of the stoichiometry of the treated films are only representative of the surface layers of the film. Given the nature of the reactive electron-beam deposition technique, it is unlikely that the composition of the r-SnO_x film before the UV–ozone treatment varied significantly as a function of depth in the film. Furthermore, the UV–ozone treatment used is likely to mainly affect the surface composition of the film. We speculate, therefore, that there may be a greater deficiency of oxygen within the bulk of the UV–ozone-treated film, however, this cannot be determined using XPS as it is unable to probe deeper into a film. We note however that the bulk composition of the r-SnO_x is not expected to substantially affect its ETL functionality, as this is mainly dictated by surface chemistry. It has been previously established that a UV–ozone treatment can greatly improve solar cell efficiency by increasing precursor solution wettability which improves surface coverage of perovskite, while also reducing the density of oxygen vacancies. Comparative studies have also shown that a UV–ozone treatment applied to a metal oxide ETL can improve the efficiency of a PSC device by over 3% compared to a device using an equivalent untreated film.^[69,70] In fact, we found that untreated devices made with an r-SnO_x ETL were nonfunctional as solar cells, whereas those based on a UV–ozone-treated r-SnO_x film had PCEs up to 19.3%. The fact

that our champion devices are comparable to those made using nanoparticle SnO₂ demonstrates that it is the surface properties of the ETL that appear to dominate device performance.

The optical transmission measurements used here to calculate bandgaps probe the entire bulk of the film. These were recorded on thicker r-SnO_x films (85 nm) than are typically used in optimized devices to allow us to accurately identify the spectral location of the absorption edge. Here, we determine effective bandgaps of 3.46 and 3.56 eV for the untreated and UV–ozone-treated films, respectively. For the untreated surface, we expect that this should accurately reflect the bandgap of the bulk film as we do not expect differences between the bandgap of the surface and the bulk. However, for the UV–ozone-treated film, we expect that the bandgap of the surface layer may well be higher than that of the bulk resulting from the higher oxygen content, with the value of the bandgap determined by transmission measurements not accurately reflecting the actual bandgap of the surface layer. Nevertheless, we suspect that the surface of UV–ozone film may not be fully stoichiometric.

In this study, solar cell devices were made using r-SnO_x and np-SnO₂ as electron transporting layers, and it was found that r-SnO_x-based devices had a greater degree of hysteresis between forward and reverse *JV* sweeps. This effect was most evident in larger area devices. It was also found that light soaking effects were evident in r-SnO_x-based devices, with output power only stabilizing after around 20 s of light exposure. We speculate that hysteresis and light soaking effects may result from oxygen vacancies at the ETL/perovskite interface (resulting from the sub-stoichiometric surface) which act as trap states. Here, charge carriers become trapped under forward bias conditions and are then released under reverse bias, resulting in the greater observed current. Light soaking during the stabilized efficiency measurements is also expected to populate such states over time and thus increase device efficiency. We expect that the density of trap states could be reduced using additional post-deposition treatments such as thermal annealing, as has been applied to other ETLs such as TiO₂.^[71] However, such techniques are unlikely to be applicable with sensitive polymeric substrates.

4. Conclusions

We have described a method by which films of tin oxide can be deposited via a low-temperature reactive electron-beam evaporation technique followed by the application of a post-deposition UV–ozone treatment. Using XRD measurements, we have confirmed that the films are amorphous, with XPS measurements demonstrating that the UV–ozone treatment increases the ratio of oxygen to tin at the surface from 1.26 to 1.74. Thin films deposited via this method were used as an ETL in PSCs based on a standard (n-i-p) architecture and compared to those utilizing an ETL deposited via colloidal tin oxide nanoparticles. In general, both types of devices had similar performance metrics, with champion devices for both nanoparticle and reactive tin oxide devices having remarkably similar values of PCE, *V*_{oc}, *J*_{sc}, and *FF*. However, devices incorporating the ETL deposited by the reactive deposition process had a broader distribution of all four performance metrics together with a greater degree of hysteresis in the *J–V* curves. Nevertheless, we believe the use of reactive

electron-beam deposition to deposit the ETL has numerous advantages over a process involving the use of a colloidal nanoparticle solution, such as the presence of additives in the colloidal solution that has been shown to reduce solar cell stability. We also observed similar degradation rates of devices containing the electron-beam deposited tin oxide under illumination to their nanoparticle equivalents. We believe the reactive process is also superior to other reported deposition methods in terms of its compatibility with sensitive plastic substrates. Although the UV–ozone exposure step applied here is relatively slow (taking 20 min), we expect that this process could be accelerated by using a higher power UV source, with further experiments planned to explore this issue. We believe, therefore, that the reactive electron-beam process described here has potential as a low temperature, high throughput method for depositing tin oxide layers for roll-to-roll printing of highly efficient PSCs.

Supporting Information

Supporting Information is available from the Wiley Online Library or from the author.

Acknowledgements

This work was funded by Power Roll Ltd and by the Engineering and Physical Sciences Research Council (EPSRC) grant EP/S009213/1 (The integration of photovoltaic devices with carbon–fiber composites). D.B. thanks Power Roll for co-funding his Ph.D. studentship. M.O.K. thanks the EPSRC for a Ph.D. studentship from the Centre for Doctoral Training in Polymers, Soft Matter and Colloids, EP/L016281/1. The authors also thank Dr Deborah Hammond at the Sheffield Surface Analysis Centre for her help with the XPS data.

Conflict of Interest

David Lidzey is a director and shareholder of the materials science company Ossila Ltd that retails equipment and materials (including perovskite semiconductors) for photovoltaic device research. Power Roll Ltd are developing a novel V-groove based photovoltaic device architecture that incorporates metal-oxide charge transport layers similar to those explored in this work.

Data Availability Statement

The data that support the findings of this study are openly available in ORDA at 10.15131/shef.data.c.5990458.

Keywords

perovskites, photovoltaic devices, solar cells, tin oxide, electron beam, deposition, electron-transport-layers

Received: March 23, 2022

Revised: May 16, 2022

Published online:

[1] A. Kojima, K. Teshima, Y. Shirai, T. Miyasaka, *J. Am. Chem. Soc.* **2009**, *131*, 6050.

[2] N. R. E. Laboratory, Best Research-Cell Efficiency Chart (accessed: October 2021).

- [3] J. J. Yoo, G. Seo, M. R. Chua, T. G. Park, Y. Lu, F. Rotermund, Y.-K. Kim, C. S. Moon, N. J. Jeon, J.-P. Correa-Baena, V. Bulović, S. S. Shin, M. G. Bawendi, J. Seo, *Nature* **2021**, *590*, 587.
- [4] J. Jeong, M. Kim, J. Seo, H. Lu, P. Ahlawat, A. Mishra, Y. Yang, M. A. Hope, F. T. Eickemeyer, M. Kim, Y. J. Yoon, I. W. Choi, B. P. Darwich, S. J. Choi, Y. Jo, J. H. Lee, B. Walker, S. M. Zakeeruddin, L. Emsley, U. Rothlisberger, A. Hagfeldt, D. S. Kim, M. Grätzel, J. Y. Kim, *Nature* **2021**, *592*, 381.
- [5] E. M. Hutter, G. E. Eperon, S. D. Stranks, T. J. Savenije, *J. Phys. Chem. Lett.* **2015**, *6*, 3082.
- [6] H.-S. Duan, H. Zhou, Q. Chen, P. Sun, S. Luo, T.-B. Song, B. Bob, Y. Yang, *Phys. Chem. Chem. Phys.* **2015**, *17*, 112.
- [7] G. Xing, N. Mathews, S. S. Lim, N. Yantara, X. Liu, D. Sabba, M. Grätzel, S. Mhaisalkar, T. C. Sum, *Nat. Mater.* **2014**, *13*, 476.
- [8] B. Chen, S.-W. Baek, Y. Hou, E. Aydin, M. De Bastiani, B. Scheffel, A. Proppe, Z. Huang, M. Wei, Y.-K. Wang, E.-H. Jung, T. G. Allen, E. Van Kerschaver, F. P. García De Arquer, M. I. Saidaminov, S. Hoogland, S. De Wolf, E. H. Sargent, *Nat. Commun.* **2020**, *11*, article no. 1257.
- [9] S. Liu, Y. Guan, Y. Sheng, Y. Hu, Y. Rong, A. Mei, H. Han, *Adv. Mater.* **2020**, *10*, 1902492.
- [10] T. M. Brenner, D. A. Egger, L. Kronik, G. Hodes, D. Cahen, *Nat. Rev. Mater.* **2016**, *1*, 15007.
- [11] J.-W. Lee, D.-J. Seol, A.-N. Cho, N.-G. Park, *Adv. Mater.* **2014**, *26*, 4991.
- [12] J.-H. Im, C.-R. Lee, J.-W. Lee, S.-W. Park, N.-G. Park, *Nanoscale* **2011**, *3*, 4088.
- [13] Q. Dong, Y. Fang, Y. Shao, P. Mulligan, J. Qiu, L. Cao, J. Huang, *Science* **2015**, *347*, 967.
- [14] G. Xing, N. Mathews, S. Sun, S. S. Lim, Y. M. Lam, M. Grätzel, S. Mhaisalkar, T. C. Sum, *Science* **2013**, *342*, 344.
- [15] S. D. Stranks, G. E. Eperon, G. Grancini, C. Menelaou, M. J. P. Alcocer, T. Leijtens, L. M. Herz, A. Petrozza, H. J. Snaith, *Science* **2013**, *342*, 341.
- [16] W. Zhang, G. E. Eperon, H. J. Snaith, *Nat. Energy* **2016**, *1*, 16048.
- [17] N. J. Jeon, J. H. Noh, W. S. Yang, Y. C. Kim, S. Ryu, J. Seo, S. I. Seok, *Nature* **2015**, *517*, 476.
- [18] A. Jain, H. Tan, O. Voznyy, X. Lan, F. P. García de Arquer, J. Z. Fan, R. Quintero-Bermudez, M. Yuan, B. Zhang, Y. Zhao, F. Fan, P. Li, L. N. Quan, Y. Zhao, Z. H. Lu, Z. Yang, S. Hoogland, E. H. Sargent, *Science* **2017**, *355*, 722.
- [19] J. Teuscher, M. M. Lee, T. Miyasaka, T. N. Murakami, H. J. Snaith, *Science* **2012**, *338*, 643.
- [20] H.-S. Kim, C.-R. Lee, J.-H. Im, K.-B. Lee, T. Moehl, A. Marchioro, S.-J. Moon, R. Humphry-Baker, J.-H. Yum, J. E. Moser, M. Grätzel, N.-G. Park, *Sci. Rep.* **2012**, *2*, article no. 591.
- [21] H. K. Min, M. Kim, S.-U. Lee, H. Kim, G. Kim, K. Choi, J. H. Lee, S. I. Seok, *Science* **2019**, *366*, 749.
- [22] T. Leijtens, G. E. Eperon, S. Pathak, A. Abate, M. M. Lee, H. J. Snaith, *Nat. Commun.* **2013**, *4*, article no. 1885.
- [23] K. Mahmood, S. Sarwar, M. T. Mehran, *RSC Adv.* **2017**, *7*, 17044.
- [24] X. Zheng, Y. Hou, C. Bao, J. Yin, F. Yuan, Z. Huang, K. Song, J. Liu, J. Troughton, N. Gasparini, C. Zhou, Y. Lin, D.-J. Xue, B. Chen, A. K. Johnston, N. Wei, M. N. Hedhili, M. Wei, A. Y. Alsalloum, P. Maity, B. Turedi, C. Yang, D. Baran, T. D. Anthopoulos, Y. Han, Z.-H. Lu, O. F. Mohammed, F. Gao, E. H. Sargent, O. M. Bakr, *Nat. Energy* **2020**, *5*, 131.
- [25] Z. Huang, D. Ouyang, C. J. Shih, B. Yang, W. C. H. Choy, *Adv. Mater.* **2020**, *10*, 1900903.
- [26] Z.-K. Wang, L.-S. Liao, *Adv. Opt. Mater.* **2018**, *6*, 1800276.
- [27] B. Roose, Q. Wang, A. Abate, *Adv. Mater.* **2018**, *9*, 1803140.

- [28] J. A. Christians, P. Schulz, J. S. Tinkham, T. H. Schloemer, S. P. Harvey, B. J. Tremolet De Villers, A. Sellinger, J. J. Berry, J. M. Luther, *Nat. Energy* **2018**, *3*, 68.
- [29] J. P. Correa Baena, L. Steier, W. Tress, M. Saliba, S. Neutzner, T. Matsui, F. Giordano, T. J. Jacobsson, A. R. Srimath Kandada, S. M. Zakeeruddin, A. Petrozza, A. Abate, M. K. Nazeeruddin, M. Grätzel, A. Hagfeldt, *Energy Environ. Sci.* **2015**, *8*, 2928.
- [30] T. Zhou, H. Lai, T. Liu, D. Lu, X. Wan, X. Zhang, Y. Liu, Y. Chen, *Adv. Mater.* **2019**, *31*, 1901242.
- [31] Q. Jiang, Z. Chu, P. Wang, X. Yang, H. Liu, Y. Wang, Z. Yin, J. Wu, X. Zhang, J. You, *Adv. Mater.* **2017**, *29*, 1703852.
- [32] D. Yang, R. Yang, K. Wang, C. Wu, X. Zhu, J. Feng, X. Ren, G. Fang, S. Priya, S. Liu, *Nat. Commun.* **2018**, *9*, article no. 3239.
- [33] Q. Jiang, Y. Zhao, X. Zhang, X. Yang, Y. Chen, Z. Chu, Q. Ye, X. Li, Z. Yin, J. You, *Nat. Photon.* **2019**, *13*, 460.
- [34] C. Altinkaya, E. Aydin, E. Ugur, F. H. Isikgor, A. S. Subbiah, M. De Bastiani, J. Liu, A. Babayigit, T. G. Allen, F. Laquai, A. Yildiz, S. De Wolf, *Adv. Mater.* **2021**, *33*, 2005504.
- [35] L. Zuo, H. Guo, D. W. Dequillettes, S. Jariwala, N. De Marco, S. Dong, R. Deblock, D. S. Ginger, B. Dunn, M. Wang, Y. Yang, *Sci. Adv.* **2017**, *3*, e1700106.
- [36] W. Ke, G. Fang, Q. Liu, L. Xiong, P. Qin, H. Tao, J. Wang, H. Lei, B. Li, J. Wan, G. Yang, Y. Yan, *J. Am. Chem. Soc.* **2015**, *137*, 6730.
- [37] J. Li, H. Wang, X. Y. Chin, H. A. Dewi, K. Vergeer, T. W. Goh, J. W. M. Lim, J. H. Lew, K. P. Loh, C. Soci, T. C. Sum, H. J. Bolink, N. Mathews, S. Mhaisalkar, A. Bruno, *Joule* **2020**, *4*, 1035.
- [38] M. F. Mohamad Noh, N. A. Arzaee, J. Safaei, N. A. Mohamed, H. P. Kim, A. R. Mohd Yusoff, J. Jang, M. A. Mat Teridi, *J. Alloys Compd.* **2019**, *773*, 997.
- [39] M. Wong-Stringer, T. J. Routledge, T. McArdle, C. J. Wood, O. S. Game, J. A. Smith, J. E. Bishop, N. Vaenas, D. M. Coles, A. R. Buckley, D. G. Lidzey, *Energy Environ. Sci.* **2019**, *12*, 1928.
- [40] C. Liang, Z. Wu, P. Li, J. Fan, Y. Zhang, G. Shao, *Appl. Surf. Sci.* **2017**, *391*, 337.
- [41] J.-P. Correa-Baena, W. Tress, K. Domanski, E. H. Anaraki, S.-H. Turren-Cruz, B. Roose, P. P. Boix, M. Grätzel, M. Saliba, A. Abate, A. Hagfeldt, *Energy Environ. Sci.* **2017**, *10*, 1207.
- [42] S. Seo, S. Jeong, H. Park, H. Shin, N.-G. Park, *Chem. Commun.* **2019**, *55*, 2403.
- [43] Y. Lv, P. Xu, G. Ren, F. Chen, H. Nan, R. Liu, D. Wang, X. Tan, X. Liu, H. Zhang, Z.-K. Chen, *ACS Appl. Mater. Interfaces* **2018**, *10*, 23928.
- [44] J. A. Smith, O. S. Game, J. E. Bishop, E. L. K. Spooner, R. C. Kilbride, C. Greenland, R. Jayaprakash, T. I. Alanazi, E. J. Cassella, A. Tejada, G. Chistiakova, M. Wong-Stringer, T. J. Routledge, A. J. Parnell, D. B. Hammond, D. G. Lidzey, *ACS Appl. Energy Mater.* **2020**, *3*, 5552.
- [45] Q. Jiang, L. Zhang, H. Wang, X. Yang, J. Meng, H. Liu, Z. Yin, J. Wu, X. Zhang, J. You, *Nat. Energy* **2017**, *2*, 16177.
- [46] T. Bu, J. Li, F. Zheng, W. Chen, X. Wen, Z. Ku, Y. Peng, J. Zhong, Y.-B. Cheng, F. Huang, *Nat. Commun.* **2018**, *9*, article no. 4609.
- [47] L. Gao, K. Huang, C. Long, F. Zeng, B. Liu, J. Yang, *Appl. Phys. A* **2020**, *126*, article no. 452.
- [48] F. Di Giacomo, S. Shanmugam, H. Fledderus, B. J. Bruijinaers, W. J. H. Verhees, M. S. Dorenkamper, S. C. Veenstra, W. Qiu, R. Gehlhaar, T. Merckx, T. Aernouts, R. Andriessen, Y. Galagan, *Sol. Energy Mater. Sol. Cells* **2018**, *181*, 53.
- [49] J. B. Whitaker, D. H. Kim, B. W. Larson, F. Zhang, J. J. Berry, M. F. A. M. Van Hest, K. Zhu, *Sustainable Energy Fuels* **2018**, *2*, 2442.
- [50] Y. Peng, F. Zeng, Y. Cheng, C. Wang, K. Huang, P. Xie, H. Xie, Y. Gao, J. Yang, *Org. Electron.* **2020**, *83*, 105736.
- [51] X. Chang, J. Fang, Y. Fan, T. Luo, H. Su, Y. Zhang, J. Lu, L. Tsetseris, T. D. Anthopoulos, S. Liu, K. Zhao, *Adv. Mater.* **2020**, *32*, 2001243.
- [52] T. I. Alanazi, O. S. Game, J. A. Smith, R. C. Kilbride, C. Greenland, R. Jayaprakash, K. Georgiou, N. J. Terrill, D. G. Lidzey, *RSC Adv.* **2020**, *10*, 40341.
- [53] L. Qiu, Z. Liu, L. K. Ono, Y. Jiang, D. Y. Son, Z. Hawash, S. He, Y. Qi, *Adv. Funct. Mater.* **2019**, *29*, 1806779.
- [54] G. Bai, Z. Wu, J. Li, T. Bu, W. Li, W. Li, F. Huang, Q. Zhang, Y.-B. Cheng, J. Zhong, *Sol. Energy* **2019**, *183*, 306.
- [55] Y. Guo, X. Yin, J. Liu, W. Chen, S. Wen, M. Que, H. Xie, Y. Yang, W. Que, B. Gao, *Org. Electron.* **2019**, *65*, 207.
- [56] Z. Chen, G. Yang, X. Zheng, H. Lei, C. Chen, J. Ma, H. Wang, G. Fang, *J. Power Sources* **2017**, *351*, 123.
- [57] J. Ma, X. Zheng, H. Lei, W. Ke, C. Chen, Z. Chen, G. Yang, G. Fang, *Sol. RRL* **2017**, *1*, 1700118.
- [58] T. J. Routledge, M. Wong-Stringer, O. S. Game, J. A. Smith, J. E. Bishop, N. Vaenas, B. G. Freestone, D. M. Coles, T. McArdle, A. R. Buckley, D. G. Lidzey, *J. Mater. Chem. A* **2019**, *7*, 2283.
- [59] Z. Song, C. L. McElvany, A. B. Phillips, I. Celik, P. W. Krantz, S. C. Waththage, G. K. Liyanage, D. Apul, M. J. Heben, *Energy Environ. Sci.* **2017**, *10*, 1297.
- [60] J. Gong, S. B. Darling, F. You, *Energy Environ. Sci.* **2015**, *8*, 1953.
- [61] S. Sajid, A. M. Elseman, H. Huang, J. Ji, S. Dou, H. Jiang, X. Liu, D. Wei, P. Cui, M. Li, *Nano Energy* **2018**, *51*, 408.
- [62] S. Y. Turishchev, O. A. Chuvenkova, E. V. Parinova, D. A. Koyuda, R. G. Chumakov, M. Presselt, A. Schleusener, V. Sivakov, *Results Phys.* **2018**, *11*, 507.
- [63] M. Fujishima, Q. Jin, H. Yamamoto, H. Tada, M. Nolan, *Phys. Chem. Chem. Phys.* **2012**, *14*, 705.
- [64] D. H. Wang, A. K. K. Kyaw, V. Gupta, G. C. Bazan, A. J. Heeger, *Adv. Mater.* **2013**, *3*, 1161.
- [65] M. Saliba, L. Etgar, *ACS Energy Lett.* **2020**, *5*, 2886.
- [66] M. G. Mason, L. S. Hung, C. W. Tang, S. T. Lee, K. W. Wong, M. Wang, *J. Appl. Phys.* **1999**, *86*, 1688.
- [67] W. Song, S. K. So, D. Wang, Y. Qiu, L. Cao, *Appl. Surf. Sci.* **2001**, *177*, 158.
- [68] J. B. Gilbert, M. F. Rubner, R. E. Cohen, *Proc. Natl. Acad. Sci.* **2013**, *110*, 6651.
- [69] P. F. Méndez, S. K. M. Muhammed, E. M. Barea, S. Masi, I. Mora-Seró, *Sol. RRL* **2019**, *3*, 1900191.
- [70] Z. Wang, J. Fang, Y. Mi, X. Zhu, H. Ren, X. Liu, Y. Yan, *Appl. Surf. Sci.* **2018**, *436*, 596.
- [71] S. Boukrouh, R. Bensaha, S. Bourgeois, E. Finot, M. C. Marco De Lucas, *Thin Solid Films* **2008**, *516*, 6353.